Research Article | Vol. 8, No. 1 | 1 Jan 2017 | BIOMEDICAL OPTICS EXPRESS 193

Biomedical Optics EXPRESS

Simultaneous multimodal ophthalmic imaging using swept-source spectrally encoded scanning laser ophthalmoscopy and optical coherence tomography

JOSEPH D. MALONE,[1,2] MOHAMED T. EL-HADDAD,[1,2] IVAN BOZIC,[1,2] LOGAN A. TYE,[3] LUCAS MAJEAU,[4] NICOLAS GODBOUT,[4,5] ANDREW M. ROLLINS,[3] CAROLINE BOUDOUX,[4,5] KAREN M. JOOS,[1,6] SHRIJI N. PATEL,[6] AND YUANKAI K. TAO[1,2,*]

[1]*Current Affiliation: Department of Biomedical Engineering, Vanderbilt University, Nashville, TN 37235, USA*
[2]*Previous Affiliation: Ophthalmic Imaging Center, Cole Eye Institute, Cleveland Clinic, Cleveland, OH 44195, USA*
[3]*Department of Biomedical Engineering, Case Western Reserve University, Cleveland, OH 44106, USA*
[4]*Castor Optics, Montreal, QC H3T 2B1, Canada*
[5]*Centre d'Optique Photonique et Lasers, Polytechnique Montreal, Department of Engineering Physics, Montreal, QC H3C 3A7, Canada*
[6]*Department of Ophthalmology and Visual Sciences, Vanderbilt University, Nashville, TN 37235, USA*
[*]*yuankai.tao@vanderbilt.edu*

Abstract: Scanning laser ophthalmoscopy (SLO) benefits diagnostic imaging and therapeutic guidance by allowing for high-speed *en face* imaging of retinal structures. When combined with optical coherence tomography (OCT), SLO enables real-time aiming and retinal tracking and provides complementary information for post-acquisition volumetric co-registration, bulk motion compensation, and averaging. However, multimodality SLO-OCT systems generally require dedicated light sources, scanners, relay optics, detectors, and additional digitization and synchronization electronics, which increase system complexity. Here, we present a multimodal ophthalmic imaging system using swept-source spectrally encoded scanning laser ophthalmoscopy and optical coherence tomography (SS-SESLO-OCT) for *in vivo* human retinal imaging. SESLO reduces the complexity of *en face* imaging systems by multiplexing spatial positions as a function of wavelength. SESLO image quality benefited from single-mode illumination and multimode collection through a prototype double-clad fiber coupler, which optimized scattered light throughput and reduce speckle contrast while maintaining lateral resolution. Using a shared 1060 nm swept-source, shared scanner and imaging optics, and a shared dual-channel high-speed digitizer, we acquired inherently co-registered *en face* retinal images and OCT cross-sections simultaneously at 200 frames-per-second.

OCIS codes: (110.4500) Optical coherence tomography; (170.5755) Retina scanning; (170.4460) Ophthalmic optics and devices.

References and links

1. D. Huang, E. A. Swanson, C. P. Lin, J. S. Schuman, W. G. Stinson, W. Chang, M. R. Hee, T. Flotte, K. Gregory, C. A. Puliafito, and et, "Optical coherence tomography," Science **254**(5035), 1178–1181 (1991).
2. C. A. Puliafito, M. R. Hee, C. P. Lin, E. Reichel, J. S. Schuman, J. S. Duker, J. A. Izatt, E. A. Swanson, and J. G. Fujimoto, "Imaging of macular diseases with optical coherence tomography," Ophthalmology **102**(2), 217–229 (1995).
3. J. A. Goldsmith, Y. Li, M. R. Chalita, V. Westphal, C. A. Patil, A. M. Rollins, J. A. Izatt, and D. Huang, "Anterior chamber width measurement by high-speed optical coherence tomography," Ophthalmology **112**(2), 238–244 (2005).
4. W. Drexler, U. Morgner, R. K. Ghanta, F. X. Kärtner, J. S. Schuman, and J. G. Fujimoto, "Ultrahigh-resolution ophthalmic optical coherence tomography," Nat. Med. **7**(4), 502–507 (2001).
5. M. Stopa, B. A. Bower, E. Davies, J. A. Izatt, and C. A. Toth, "Correlation of pathologic features in spectral domain optical coherence tomography with conventional retinal studies," Retina **28**(2), 298–308 (2008).

#278530 http://dx.doi.org/10.1364/BOE.8.000193
Journal © 2017 Received 10 Oct 2016; revised 6 Dec 2016; accepted 7 Dec 2016; published 12 Dec 2016

Biomedical Optics EXPRESS

6. M. R. Hee, C. R. Baumal, C. A. Puliafito, J. S. Duker, E. Reichel, J. R. Wilkins, J. G. Coker, J. S. Schuman, E. A. Swanson, and J. G. Fujimoto, "Optical coherence tomography of age-related macular degeneration and choroidal neovascularization," Ophthalmology **103**(8), 1260–1270 (1996).
7. M. R. Hee, C. A. Puliafito, J. S. Duker, E. Reichel, J. G. Coker, J. R. Wilkins, J. S. Schuman, E. A. Swanson, and J. G. Fujimoto, "Topography of diabetic macular edema with optical coherence tomography," Ophthalmology **105**(2), 360–370 (1998).
8. O. Tan, V. Chopra, A. T. Lu, J. S. Schuman, H. Ishikawa, G. Wollstein, R. Varma, and D. Huang, "Detection of macular ganglion cell loss in glaucoma by Fourier-domain optical coherence tomography," Ophthalmology **116**, 2305 (2009).
9. R. L. Avery, D. J. Pieramici, M. D. Rabena, A. A. Castellarin, M. A. Nasir, and M. J. Giust, "Intravitreal bevacizumab (Avastin) for neovascular age-related macular degeneration," Ophthalmology **113**(3), 363–372 (2006).
10. P. J. Rosenfeld, A. E. Fung, and C. A. Puliafito, "Optical coherence tomography findings after an intravitreal injection of bevacizumab (avastin) for macular edema from central retinal vein occlusion," Ophthalmic Surg. Lasers Imaging **36**(4), 336–339 (2005).
11. D. F. Martin, M. G. Maguire, G. S. Ying, J. E. Grunwald, S. L. Fine, and G. J. Jaffe; CATT Research Group, "Ranibizumab and bevacizumab for neovascular age-related macular degeneration," N. Engl. J. Med. **364**(20), 1897–1908 (2011).
12. I. Grulkowski, J. J. Liu, B. Potsaid, V. Jayaraman, C. D. Lu, J. Jiang, A. E. Cable, J. S. Duker, and J. G. Fujimoto, "Retinal, anterior segment and full eye imaging using ultrahigh speed swept source OCT with vertical-cavity surface emitting lasers," Biomed. Opt. Express **3**(11), 2733–2751 (2012).
13. B. Potsaid, B. Baumann, D. Huang, S. Barry, A. E. Cable, J. S. Schuman, J. S. Duker, and J. G. Fujimoto, "Ultrahigh speed 1050nm swept source/Fourier domain OCT retinal and anterior segment imaging at 100,000 to 400,000 axial scans per second," Opt. Express **18**(19), 20029–20048 (2010).
14. T. Klein, W. Wieser, L. Reznicek, A. Neubauer, A. Kampik, and R. Huber, "Multi-MHz retinal OCT," Biomed. Opt. Express **4**(10), 1890–1908 (2013).
15. T. Klein, W. Wieser, C. M. Eigenwillig, B. R. Biedermann, and R. Huber, "Megahertz OCT for ultrawide-field retinal imaging with a 1050 nm Fourier domain mode-locked laser," Opt. Express **19**(4), 3044–3062 (2011).
16. J. P. Kolb, T. Klein, C. L. Kufner, W. Wieser, A. S. Neubauer, and R. Huber, "Ultra-widefield retinal MHz-OCT imaging with up to 100 degrees viewing angle," Biomed. Opt. Express **6**(5), 1534–1552 (2015).
17. L. Reznicek, T. Klein, W. Wieser, M. Kernt, A. Wolf, C. Haritoglou, A. Kampik, R. Huber, and A. S. Neubauer, "Megahertz ultra-wide-field swept-source retina optical coherence tomography compared to current existing imaging devices," Graefes Arch. Clin. Exp. Ophthalmol. **252**(6), 1009–1016 (2014).
18. R. P. McNabb, D. S. Grewal, S. Schuman, P. Mruthyunjaya, J. A. Izatt, and A. N. Kuo, "Ultra wide-field swept-source optical coherence tomography for peripheral eye disease," Invest. Ophthalmol. Vis. Sci. **56**, 2804 (2015).
19. LIA, "American National Standard for Safe Use of Lasers," ANSI Z136.1–2014 (2014).
20. Y. Jia, O. Tan, J. Tokayer, B. Potsaid, Y. Wang, J. J. Liu, M. F. Kraus, H. Subhash, J. G. Fujimoto, J. Hornegger, and D. Huang, "Split-spectrum amplitude-decorrelation angiography with optical coherence tomography," Opt. Express **20**(4), 4710–4725 (2012).
21. L. An and R. K. Wang, "In vivo volumetric imaging of vascular perfusion within human retina and choroids with optical micro-angiography," Opt. Express **16**(15), 11438–11452 (2008).
22. Y. K. Tao, K. M. Kennedy, and J. A. Izatt, "Velocity-resolved 3D retinal microvessel imaging using single-pass flow imaging spectral domain optical coherence tomography," Opt. Express **17**(5), 4177–4188 (2009).
23. Y. Wang, B. A. Bower, J. A. Izatt, O. Tan, and D. Huang, "Retinal blood flow measurement by circumpapillary Fourier domain Doppler optical coherence tomography," J. Biomed. Opt. **13**(6), 064003 (2008).
24. S. Makita, Y. Hong, M. Yamanari, T. Yatagai, and Y. Yasuno, "Optical coherence angiography," Opt. Express **14**(17), 7821–7840 (2006).
25. J. Fingler, R. J. Zawadzki, J. S. Werner, D. Schwartz, and S. E. Fraser, "Volumetric microvascular imaging of human retina using optical coherence tomography with a novel motion contrast technique," Opt. Express **17**(24), 22190–22200 (2009).
26. A. Mariampillai, B. A. Standish, E. H. Moriyama, M. Khurana, N. R. Munce, M. K. Leung, J. Jiang, A. Cable, B. C. Wilson, I. A. Vitkin, and V. X. Yang, "Speckle variance detection of microvasculature using swept-source optical coherence tomography," Opt. Lett. **33**(13), 1530–1532 (2008).
27. W. Choi, E. M. Moult, N. K. Waheed, M. Adhi, B. Lee, C. D. Lu, T. E. de Carlo, V. Jayaraman, P. J. Rosenfeld, J. S. Duker, and J. G. Fujimoto, "Ultrahigh-Speed, Swept-Source Optical Coherence Tomography Angiography in Nonexudative Age-Related Macular Degeneration with Geographic Atrophy," Ophthalmology **122**(12), 2532–2544 (2015).
28. Y. Jia, S. T. Bailey, D. J. Wilson, O. Tan, M. L. Klein, C. J. Flaxel, B. Potsaid, J. J. Liu, C. D. Lu, M. F. Kraus, J. G. Fujimoto, and D. Huang, "Quantitative optical coherence tomography angiography of choroidal neovascularization in age-related macular degeneration," Ophthalmology **121**(7), 1435–1444 (2014).
29. Y. Jia, S. T. Bailey, T. S. Hwang, S. M. McClintic, S. S. Gao, M. E. Pennesi, C. J. Flaxel, A. K. Lauer, D. J. Wilson, J. Hornegger, J. G. Fujimoto, and D. Huang, "Quantitative optical coherence tomography angiography of vascular abnormalities in the living human eye," Proc. Natl. Acad. Sci. U.S.A. **112**(18), E2395–E2402 (2015).
30. H. C. Hendargo, R. Estrada, S. J. Chiu, C. Tomasi, S. Farsiu, and J. A. Izatt, "Automated non-rigid registration and mosaicing for robust imaging of distinct retinal capillary beds using speckle variance optical coherence tomography," Biomed. Opt. Express **4**(6), 803–821 (2013).

Biomedical Optics EXPRESS

31. D. Y. Kim, J. Fingler, R. J. Zawadzki, S. S. Park, L. S. Morse, D. M. Schwartz, S. E. Fraser, and J. S. Werner, "Optical imaging of the chorioretinal vasculature in the living human eye," Proc. Natl. Acad. Sci. U.S.A. **110**(35), 14354–14359 (2013).
32. Q. Zhang, C. S. Lee, J. Chao, C. L. Chen, T. Zhang, U. Sharma, A. Zhang, J. Liu, K. Rezaei, K. L. Pepple, R. Munsen, J. Kinyoun, M. Johnstone, R. N. Van Gelder, and R. K. Wang, "Wide-field optical coherence tomography based microangiography for retinal imaging," Sci. Rep. **6**, 22017 (2016).
33. M. F. Kraus, B. Potsaid, M. A. Mayer, R. Bock, B. Baumann, J. J. Liu, J. Hornegger, and J. G. Fujimoto, "Motion correction in optical coherence tomography volumes on a per A-scan basis using orthogonal scan patterns," Biomed. Opt. Express **3**(6), 1182–1199 (2012).
34. B. Potsaid, I. Gorczynska, V. J. Srinivasan, Y. Chen, J. Jiang, A. Cable, and J. G. Fujimoto, "Ultrahigh speed spectral / Fourier domain OCT ophthalmic imaging at 70,000 to 312,500 axial scans per second," Opt. Express **16**(19), 15149–15169 (2008).
35. Q. Zhang, Y. Huang, T. Zhang, S. Kubach, L. An, M. Laron, U. Sharma, and R. K. Wang, "Wide-field imaging of retinal vasculature using optical coherence tomography-based microangiography provided by motion tracking," J. Biomed. Opt. **20**(6), 066008 (2015).
36. B. Potsaid, V. Jayaraman, J. Fujimoto, J. Jiang, P. Heim, and A. Cable, "MEMS tunable VCSEL light source for ultrahigh speed 60kHz - 1MHz axial scan rate and long range centimeter class OCT imaging," Proc. SPIE **8213**, 82130M (2012).
37. R. Huber, D. C. Adler, V. J. Srinivasan, and J. G. Fujimoto, "Fourier domain mode locking at 1050 nm for ultra-high-speed optical coherence tomography of the human retina at 236,000 axial scans per second," Opt. Lett. **32**(14), 2049–2051 (2007).
38. R. Huber, M. Wojtkowski, and J. G. Fujimoto, "Fourier Domain Mode Locking (FDML): A new laser operating regime and applications for optical coherence tomography," Opt. Express **14**(8), 3225–3237 (2006).
39. L. Reznicek, T. Klein, W. Wieser, M. Kernt, A. Wolf, C. Haritoglou, A. Kampik, R. Huber, and A. S. Neubauer, "Megahertz ultra-wide-field swept-source retina optical coherence tomography compared to current existing imaging devices," Graefes Arch. Clin. Exp. Ophthalmol. **252**(6), 1009–1016 (2014).
40. O. M. Carrasco-Zevallos, B. Keller, C. Viehland, L. Shen, M. I. Seider, J. A. Izatt, and C. A. Toth, "Optical Coherence Tomography for Retinal Surgery: Perioperative Analysis to Real-Time Four-Dimensional Image-Guided Surgery," Invest. Ophthalmol. Vis. Sci. **57**(9), OCT37–OCT50 (2016).
41. R. A. Abrams, D. E. Meyer, and S. Kornblum, "Speed and Accuracy of Saccadic Eye Movements: Characteristics of Impulse Variability in the Oculomotor System," J. Exp. Psychol. Hum. Percept. Perform. **15**(3), 529–543 (1989).
42. V. P. Laurutis and D. A. Robinson, "The Vestibulo-Ocular Reflex During Human Saccadic Eye Movements," J. Physiol. **373**(1), 209–233 (1986).
43. D. A. Robinson, "The Mechanics of Human Saccadic Eye Movement," J. Physiol. **174**(2), 245–264 (1964).
44. C. D. Lu, M. F. Kraus, B. Potsaid, J. J. Liu, W. Choi, V. Jayaraman, A. E. Cable, J. Hornegger, J. S. Duker, and J. G. Fujimoto, "Handheld ultrahigh speed swept source optical coherence tomography instrument using a MEMS scanning mirror," Biomed. Opt. Express **5**(1), 293–311 (2014).
45. D. Nankivil, G. Waterman, F. LaRocca, B. Keller, A. N. Kuo, and J. A. Izatt, "Handheld, rapidly switchable, anterior/posterior segment swept source optical coherence tomography probe," Biomed. Opt. Express **6**(11), 4516–4528 (2015).
46. R. H. Webb and G. W. Hughes, "Scanning laser ophthalmoscope," IEEE Trans. Biomed. Eng. **28**(7), 488–492 (1981).
47. R. H. Webb, G. W. Hughes, and F. C. Delori, "Confocal scanning laser ophthalmoscope," Appl. Opt. **26**(8), 1492–1499 (1987).
48. R. H. Webb, G. W. Hughes, and O. Pomerantzeff, "Flying spot TV ophthalmoscope," Appl. Opt. **19**(17), 2991–2997 (1980).
49. Y. K. Tao and J. A. Izatt, "Spectrally encoded confocal scanning laser ophthalmoscopy," Opt. Lett. **35**(4), 574–576 (2010).
50. Y. K. Tao, S. Farsiu, and J. A. Izatt, "Interlaced spectrally encoded confocal scanning laser ophthalmoscopy and spectral domain optical coherence tomography," Biomed. Opt. Express **1**(2), 431–440 (2010).
51. E. De Montigny, W. J. Madore, O. Ouellette, G. Bernard, M. Leduc, M. Strupler, C. Boudoux, and N. Godbout, "Double-clad fiber coupler for partially coherent detection," Opt. Express **23**(7), 9040–9051 (2015).
52. S. Lemire-Renaud, M. Rivard, M. Strupler, D. Morneau, F. Verpillat, X. Daxhelet, N. Godbout, and C. Boudoux, "Double-clad fiber coupler for endoscopy," Opt. Express **18**(10), 9755–9764 (2010).
53. M. Guizar-Sicairos, S. T. Thurman, and J. R. Fienup, "Efficient subpixel image registration algorithms," Opt. Lett. **33**(2), 156–158 (2008).
54. A. Zeidan and D. Yelin, "Miniature forward-viewing spectrally encoded endoscopic probe," Opt. Lett. **39**(16), 4871–4874 (2014).
55. D. Yelin, W. M. White, J. T. Motz, S. H. Yun, B. E. Bouma, and G. J. Tearney, "Spectral-domain spectrally-encoded endoscopy," Opt. Express **15**(5), 2432–2444 (2007).
56. G. J. Tearney, M. Shishkov, and B. E. Bouma, "Spectrally encoded miniature endoscopy," Opt. Lett. **27**(6), 412–414 (2002).
57. C. Boudoux, S. Yun, W. Oh, W. White, N. Iftimia, M. Shishkov, B. Bouma, and G. Tearney, "Rapid wavelength-swept spectrally encoded confocal microscopy," Opt. Express **13**(20), 8214–8221 (2005).
58. G. J. Tearney, R. H. Webb, and B. E. Bouma, "Spectrally encoded confocal microscopy," Opt. Lett. **23**(15), 1152–1154 (1998).

Biomedical Optics EXPRESS

59. O. Pomerantzeff, M. Pankratov, G. J. Wang, and P. Dufault, "Wide-angle optical model of the eye," Am. J. Optom. Physiol. Opt. **61**(3), 166–176 (1984).
60. W. J. Madore, E. De Montigny, O. Ouellette, S. Lemire-Renaud, M. Leduc, X. Daxhelet, N. Godbout, and C. Boudoux, "Asymmetric double-clad fiber couplers for endoscopy," Opt. Lett. **38**(21), 4514–4517 (2013).
61. M. Wojtkowski, V. Srinivasan, T. Ko, J. Fujimoto, A. Kowalczyk, and J. Duker, "Ultrahigh-resolution, high-speed, Fourier domain optical coherence tomography and methods for dispersion compensation," Opt. Express **12**(11), 2404–2422 (2004).
62. D. J. Fechtig, B. Grajciar, T. Schmoll, C. Blatter, R. M. Werkmeister, W. Drexler, and R. A. Leitgeb, "Line-field parallel swept source MHz OCT for structural and functional retinal imaging," Biomed. Opt. Express **6**(3), 716–735 (2015).
63. H. Spahr, D. Hillmann, C. Hain, C. Pfäffle, H. Sudkamp, G. Franke, and G. Hüttmann, "Imaging pulse wave propagation in human retinal vessels using full-field swept-source optical coherence tomography," Opt. Lett. **40**(20), 4771–4774 (2015).
64. R. Matungka, Y. F. Zheng, and R. L. Ewing, "Image registration using adaptive polar transform," IEEE Trans. Image Process. **18**(10), 2340–2354 (2009).
65. D. X. Hammer, R. D. Ferguson, T. E. Ustun, C. E. Bigelow, N. V. Iftimia, and R. H. Webb, "Line-scanning laser ophthalmoscope," J. Biomed. Opt. **11**(4), 041126 (2006).
66. D. X. Hammer, R. D. Ferguson, T. E. Ustun, G. Maislin, and R. H. Webb, "Hand-held digital line-scanning laser ophthalmoscope (LSLO)," Proc. SPIE **5314**, 161–169 (2004).
67. N. V. Iftimia, D. X. Hammer, C. E. Bigelow, T. Ustun, J. F. de Boer, and R. D. Ferguson, "Hybrid retinal imager using line-scanning laser ophthalmoscopy and spectral domain optical coherence tomography," Opt. Express **14**(26), 12909–12914 (2006).
68. P. S. Silva, J. D. Cavallerano, J. K. Sun, A. Z. Soliman, L. M. Aiello, and L. P. Aiello, "Peripheral lesions identified by mydriatic ultrawide field imaging: distribution and potential impact on diabetic retinopathy severity," Ophthalmology **120**(12), 2587–2595 (2013).
69. P. S. Silva, J. D. Cavallerano, N. M. Haddad, H. Kwak, K. H. Dyer, A. F. Omar, H. Shikari, L. M. Aiello, J. K. Sun, and L. P. Aiello, "Peripheral Lesions Identified on Ultrawide Field Imaging Predict Increased Risk of Diabetic Retinopathy Progression over 4 Years," Ophthalmology **122**(5), 949–956 (2015).
70. N. Z. Gregori, B. L. Lam, G. Gregori, S. Ranganathan, E. M. Stone, A. Morante, F. Abukhalil, and P. R. Aroucha, "Wide-Field Spectral-Domain Optical Coherence Tomography in Patients and Carriers of X-Linked Retinoschisis," Ophthalmology **120**(1), 169–174 (2013).

1. Introduction

Optical coherence tomography (OCT) [1] allows noninvasive optical imaging of ophthalmic microstructures and has widespread clinical applications including diagnostics [2–5], tracking disease progression [6–8], and therapeutic planning [9–11]. Technological advances in recent years have focused on increased imaging speed [12–14], which enables volumetric imaging of large field-of-views (FOVs) out to the mid-periphery of the retina [15–18]. However, there is still a fundamental trade-off between imaging speed and signal-to-noise ratio (SNR) in OCT. This limitation is particularly stringent in ophthalmic imaging, where the optical power incident on the retina is limited by maximum permissible exposure limits [19]. Thus, many implementations of ultrahigh speed OCT require averaging of repeated cross-sections. Higher speed also benefits functional imaging methods, such as OCT angiography (OCT-A), by reducing the effect of bulk motion and fixation artifacts to allow for contrast-free *in vivo* mapping and quantification of vascular perfusion in the retina [20–26]. When combined with image tracking/stabilization and mosaicking methods, OCT-A has demonstrated potential for aiding clinical diagnostics in age-related macular degeneration, diabetic retinopathy, and pathologies in the choroid [27–32]. However, these registration methods require either acquisition of multiple orthogonally-oriented volumes or additional eye-tracking modalities, which may increase system complexity, computational overhead, and cost [32–35].

Recent advances in swept-source technologies have led to significant increases in OCT acquisition rates [36–38]. Megahertz line-rate [16, 39] and 2-10 volumes-per-second ophthalmic imaging has been demonstrated using a multi-spot scanning approach [14] or by sub-sampling small FOVs [40]. While orders of magnitude faster than commercially available clinical ophthalmic OCT systems, <10 Hz volume-rates do not fully compensate for saccadic eye movements with velocities ranging from 100 to 500 deg./s [41–43]. Similarly, higher imaging speeds only reduce relative bulk motion between adjacent cross-sectional images, but do not directly benefit registration of out-of-plane motion during volumetric acquisition. Increased imaging speed also inherently trades-off with SNR (<90 dB theoretical shot-noise limited SNR for >6 MHz line-rates) and, thus, clinical imaging requires averaging of

Biomedical Optics EXPRESS

sequential cross-sections, which would also benefit from image tracking/stabilization. Finally, ultrahigh speed OCT systems are routinely implemented using resonant scanners to achieve desired frame-rates, which increase system complexity by necessitating detected synchronization electronics and acquisition clocks and image post-processing to compensate inherent nonlinear scan trajectories [44, 45].

Scanning laser ophthalmoscopy (SLO) provides high frame-rate *en face* images of ophthalmic structures [46–48]. We previously described a novel spectrally encoded confocal scanning laser ophthalmoscope (SECSLO) design that multiplexes spatial positions to increase imaging speeds while reducing overall system complexity as compared to conventional point-scanning confocal SLO (CSLO) [49]. By taking advantage of similarities between SECSLO and spectral domain OCT (SD-OCT) illumination and detection optics, we also demonstrated a multimodality ophthalmic imaging system that acquired an *en face* SECSLO scattering image of the retina interlaced with a co-registered OCT cross-section for real-time aiming and post-acquisition bulk motion estimation and compensation [50]. SECSLO and SD-OCT provide complementary information on transverse and axial retinal motion, respectively, which enables volumetric registration and averaging. However, these previous implementations of SECSLO were inherently noisy because each multiplexed spatial position was essentially monochromatic and, thus, the collected scattered light would interfere resulting in speckle noise. In addition, imaging speed was limited to ~10 kHz line-rate due to low optical throughput when using single-mode fiber (SMF) for illumination and collection. Finally, multimodal SECSLO and OCT imaging was achieved serially, as opposed to concurrently, because both modalities shared a detection spectrometer.

Here, we introduce a novel multimodal spectrally encoded SLO and OCT system using a 1060 nm swept-source (SS-SESLO-OCT) that overcomes limitations of our previous systems. Transition from a superluminescent diode to swept-laser enables single-pixel detection, which allows us to integrate a prototype double-clad fiber coupler (DCFC) for single-mode illumination and multimode collection through the core and inner cladding, respectively, for *en face* SLO imaging [51, 52]. Single-mode illumination maintains high lateral resolution while multimode collection increases scattered light throughput and reduces speckle contrast at the expense of confocality (hence SESLO as opposed to SECSLO). Both SESLO and OCT signals are acquired simultaneously on dual input channels of a high-speed digitizer, which allows for concurrent acquisition of an entire *en face* fundus SESLO image simultaneously with every OCT cross-section at 200 frames-per-second (fps). In post-processing, we estimated *en face* rotational and translational bulk motions from SESLO frames and applied them to register each cross-sectional OCT image using a computationally efficient Fourier domain cross-correlation approach [53] to remove inter- and intra-B-scan motions. Using complementary information from SESLO and OCT, we demonstrated multi-volumetric registration and averaging to recover regions of missing data resulting from blinks, saccades, and ocular drifts using mutual information from serially acquired volumes. We believe our multimodal SS-SESLO-OCT system can be directly applied for real-time aiming and image-guidance and multi-volumetric motion compensation, averaging, widefield mosaicking, and vascular mapping with potential applications in ophthalmic clinical diagnostics, handheld imaging, and intraoperative guidance.

2. Methods

Spectrally encoded imaging, including fiber optic probe [54–56] and free space microscopy [57, 58] and ophthalmoscopy [49, 50] implementations, has been described extensively in the literature. These previous publications include theoretical derivations of resolution and SNR, methods for resolving spectroscopic and functional contrast, and detailed descriptions of different illumination and detection schemes.

2.1 System design and optomechanical layout

SS-SESLO-OCT (Fig. 1) was implemented using a 100 kHz swept-source centered at 1060 nm with 100 nm bandwidth (SSOCT-1060, Axsun Technologies). The source was split

Biomedical Optics EXPRESS

between the SESLO and OCT arms using a 30:70 coupler, respectively (Fig. 1(a)). The SESLO arm was relayed through the single-mode core of a prototype DCFC (DC1060LEB, Castor Optics/Thorlabs), collimated, and dispersed through a 1200 lpmm volume phase holographic grating (WP-1200/840-50.8, Wasatch Photonics) to achieve 1616 spectrally resolvable spots. The resulting spectrally encoded extended source was 4-f relayed across a 4.4x demagnifying telescope to the fast-axis galvanometer scanner (G_x), and another 1.1x demagnifying 4-f relay to a 2 mm spot at the pupil plane (Fig. 1(b)).

The OCT path was split between reference and sample arms through an 80:20 coupler, respectively. A transmissive reference arm with a broadband hollow retroreflector was used to maximize optical power and spectral bandwidth throughput (Fig. 1(a)). The sample arm was collimated to a 2.7 mm diameter beam on the slow-axis galvanometer scanner (G_y). The OCT scan lens (f_s) was optimized such that when combined in 4-f with the shared relay lens (f_r), they would demagnify the OCT spot to match that of each SESLO spectral channel at both the shared fast-axis scanner and pupil planes (Fig. 1(b)). SESLO and OCT optical paths were combined at a conjugate image plane after the grating and objective lens and slow-axis scanner and scan lens, respectively. In this intermediate plane, both imaging paths were spectrally dispersed/scanned to a focused line, which were combined collinearly across the flat-edge of a D-shaped pick-off mirror. The FOVs of the two modalities were laterally offset at this pick-off mirror because the substrate was only coated to 50 µm to the edge. However, the overall effect of this offset was minimal because the plane is further demagnified to ~25 µm at the retina (Fig. 1(c)). The pick-off mirror was used in lieu of a beamsplitter to maximize optical throughput for both modalities, and the collinear optical layout ensured co-registration of the SESLO and OCT FOVs during imaging. CAD renderings of the system optomechanical layout (Fig. 2) enable better visualization of the alignment and relative orientation of SESLO and OCT optical paths and the approximate 18" x 5" system footprint.

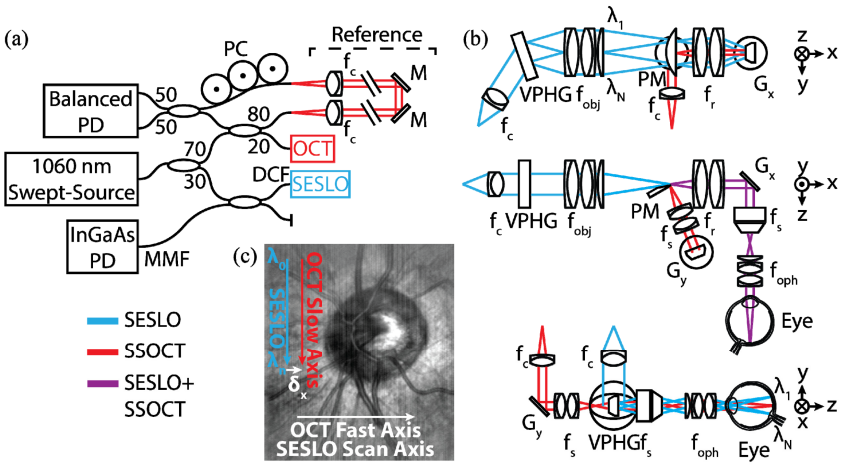

Fig. 1. SS-SESLO-OCT engine and imaging optics schematics. (a) A 1060 nm swept-source is shared between the SESLO and OCT via a 30:70 coupler, respectively. SESLO illumination is relayed by the single-mode core and detected by the multimode inner cladding of a prototype DCFC. (b) Cross-sectional views of the imaging optics (SESLO, blue; OCT, red; shared, purple). SESLO and OCT optical paths share a scanning mirror (G_x, SESLO scan axis and OCT fast axis) and are combined using a pick-off mirror. (c) Representative *in vivo* retinal SESLO image centered on the optic nerve showing: SESLO encoded, SESLO scan, OCT fast, and OCT slow axes. The SESLO and OCT FOVs are offset in the fast axis by ~25 µm at the retina (δx). DCF, double-clad fiber; f, collimating, objective, ophthalmic, relay, and scan lenses; $G_{x,y}$, galvanometer scanners; M, mirror; MMF, multimode fiber; PC, polarization controller; PD, photodiode; PM, D-shaped pickoff mirror; VPHG, grating.

Biomedical Optics EXPRESS

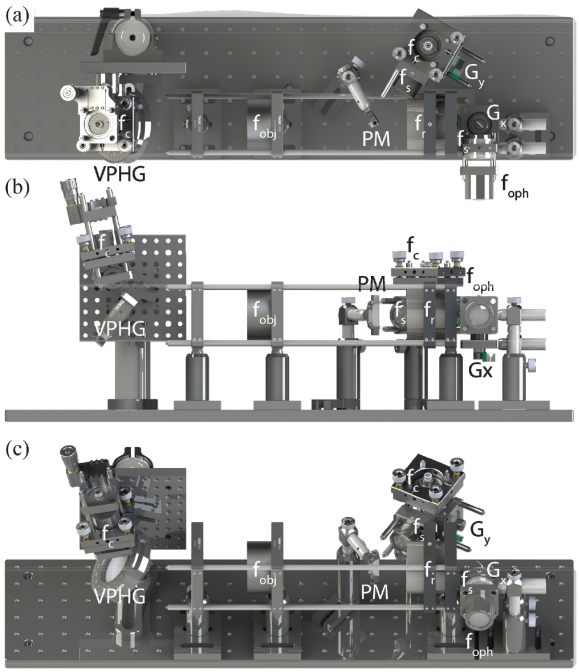

Fig. 2. SS-SESLO-OCT CAD renderings. (a) Top, (b) front, and (c) isometric views of SS-SESLO-OCT on a 6 x 24 in. optical breadboard shows the relative system size and layout, and positions of optics/optomechanics of corresponding components in Fig. 1(b). f, collimating, objective, ophthalmic, relay, and scan lenses; $G_{x,y}$, galvanometer scanners; PM, D-shaped pickoff mirror; VPHG, grating.

Imaging and relay optics were designed and optimized using OpticStudio (Zemax). Spot sizes at the retina were simulated using an eye model (Fig. 3) [59], but *in vivo* imaging resolution was ultimately limited by aberrations in the eye. For a simulated 5 mm field (Fig. 3(a), 3(c)), both SESLO and OCT have on-axis diffraction-limited spots with Airy radii of 7.56 µm and 13.8 µm, respectively. At the edges of the field, SESLO and OCT spots are 4-6x and 2-3x the Airy disc, respectively (Fig. 3(b), 3(d)). As expected, chromatic aberration resulted in asymmetric loss of spatial resolution across the SESLO FOV (Fig. 3(b)). OCT spot sizes showed non-radially symmetric loss of resolution at the retina, which was likely a result of vignetting at the input aperture of the shared scan lens (f_s, LSM02-BB, Thorlabs). The spectrally encoded FOV in SESLO is fundamentally constrained by the grating period, swept-source spectral bandwidth, and imaging relay magnification. In these simulations, SESLO scan-axis and OCT fast- and slow-axis scan angles (Fig. 1(c)) were set for isotropic imaging FOVs whereas practically, a larger anisotropic FOV may be achieved but trades-off with increased aberrations and vignetting effects.

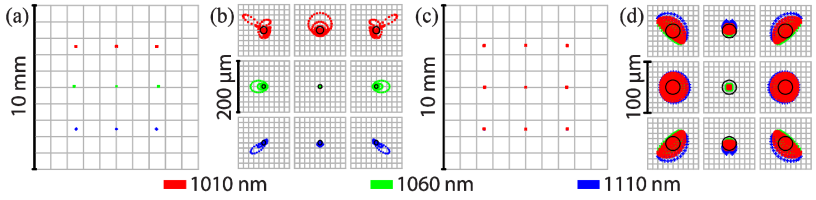

Fig. 3. SS-SESLO-OCT spot diagrams. (a), (b) SESLO and (c), (d) OCT spot diagrams showing (a), (c) full-field and (b), (d) magnified spot matrices. SESLO ray trace shows diffraction-limited performance on-axis with an Airy radius of 7.56 µm and about 4-6x the Airy disc at the edge of the field. Across a FOV matching that of the SESLO FOV, OCT spots are diffraction limited at the center of the FOV with an Airy radius of 13.8 µm and 2-3x the Airy disc at the edges of the field. All spot diagrams are simulated at the retina of a model eye.

Biomedical Optics EXPRESS

2.2 Detection and acquisition

SESLO scattered light was collected through the multimode inner cladding of the DCFC, detected using a 250 MHz InGaAs PIN photodiode (FPD510-F, MenloSystems) and 37 dB, 1.6 GHz wideband amplifier (ACA-2, Becker & Hickl). At the detector, the 200 μm multimode fiber (MMF) output of the DCFC was flat cleaved and precision aligned to the 400 μm diameter photodiode face. Multimode collection improves both SESLO optical throughput and reduces speckle contrast as compared to SMF collection [51, 52, 60]. For a double-clad fiber (DCF) with 0.2 inner cladding numerical aperture (NA) and 105 μm cladding diameter, we estimate a 1.9x theoretical reduction in overall speckle contrast. Speckle contrast can be further reduced by ensuring the modal dispersion for each spatial mode exceeds the coherence length of each spectrally encoded position. Using previously described theoretical calculations [52], we expect a 21x reduction in speckle contrast by coupling the DCF to 250 m of MMF. To reduce the background noise from fiber face reflections, the DCF input to the SESLO imaging relay was flat polished and the unused MMF port of the DCFC was coupled to a light trap filled with index-matching gel (Fig. 1).

The back-reflected OCT sample and transmissive reference arms were combined through a 50:50 coupler and detected using a 1.0 GHz InGaAs dual-balanced photodiode (PDB481C-AC, Thorlabs). Both SESLO and OCT signals were sampled simultaneously at 12 bits using dual 1.8 GS/s inputs of a high-speed digitizer (ATS9360, AlazarTech). Digitizer timing was controlled by the internal sweep-trigger and k-clock of the Axsun swept-source. Real-time acquisition, display, and data archiving software was custom-developed in C++. *En face* SESLO and cross-sectional OCT images were processed and displayed at 20 fps for real-time preview and aiming. Sample and reference paths were dispersion matched using bulk optics and fiber-optic patch cords to minimize dispersion artifacts during preview, and computational dispersion compensation was implemented in post-processing [61].

2.3 ANSI maximum permissible exposure

The limits for safe ocular exposure to laser light have been well established and are documented by the ANSI Z136.1-2014 American National Standard for the Safe Use of Lasers [19]. The most conservative maximum permissible exposure (MPE) for the 1060 nm laser radiation used in OCT will not be exceeded so long as the laser output power is below 1.9 mW. For combining contributions from multiple sources, the ANSI Standard directs that the thermal and photochemical hazards for each source should be evaluated separately as a fraction of the MPE for the particular source characteristics. The combined exposure is then considered safe if the sum of the fractional MPE from each source does not exceed unity for either the thermal or photochemical hazards. SESLO illumination is a focused, spectrally dispersed line, which may be analyzed as an extended source. For our system configuration, we calculated MPE_{SESLO} = 10.3 mW for 8 hrs of continuous imaging. While seemingly high, this value is proportional to recently published results using near infrared extended sources for retinal imaging [62, 63].

2.4 Multimodality volumetric registration using mutual information

We estimated *en face* rotational and translational bulk motions from SESLO frames and applied them to register each cross-sectional OCT image using a computationally efficient Fourier domain cross-correlation approach to remove inter- and intra-B-scan motions. Rotation was calculated by first applying adaptive log-polar transform (APT) [64] on each raw SESLO image. Similar to the log-polar transform, APT remaps the image to polar coordinates, but uses axis projection to uniformly sample the radial dimension. Rotational motions were remapped to translations in polar coordinates and estimated using a discrete Fourier transform (DFT) cross-correlation algorithm [53]. DFT cross-correlation was then applied directly to the rotationally registered images in Cartesian coordinates to estimate *en face* translational motions.

Biomedical Optics EXPRESS

OCT cross-sections were contrast-normalized and registered axially and rotationally across all volumes. Rotational and translational motions calculated from SESLO frames were then applied to corresponding OCT B-scans to compensate for inter- and intra-B-scan bulk motions. Fast- and slow-axis translation and *en face* rotation scaling factors were empirically calculated from SESLO frames and OCT volume projections. Volumetric registration was performed in post-processing using Matlab (Mathworks) and ImageJ (NIH).

3. Results

Multimodal SS-SESLO-OCT imaging was performed with 2.4 mW of SESLO and 1.4 mW of OCT optical power. The combined optical power used in this study was within the MPE for 1060 nm (*Section 2.3*). All SS-SESLO-OCT data were sampled at 1376 (SESLO/OCT spectral) x 500 (SESLO scan-axis/OCT fast-axis) pix. at 200 frames-per-second (fps). Volumetric data sets were acquired with 500 frames-per-volume in 2.5 s.

3.1 Comparison of SECSLO and SESLO imaging performance

SECSLO and SESLO images of a scattering phantom were compared to verify lateral resolution is preserved in SESLO despite using multimode collection through the inner cladding of a DCF. A USAF 1951 resolution test chart was imaged through a uniformly scattering layer at the focal plane of the shared scan lens (f_s in Fig. 1(b) and 2) to quantify lateral resolution performance (Fig. 4). A single-mode optical circulator was inserted between the SESLO arm of the 70:30 coupler and DCFC to enable SECSLO (Fig. 4(a), 4(b)) and SESLO (Fig. 4(c), 4(d)) imaging of the same resolution phantom. As expected, we observed a >3.5x increase in collection efficiency through the DCF as a result of an increased NA (DCF core: 0.12; DCF inner cladding: 0.2) and diameter (DCF core: 4 µm; DCF inner cladding: 105 µm). However, when comparing lateral resolution both SECSLO (Fig. 4(b), arrows) and SESLO (Fig. 4(d), arrows) were able to resolve identical elements.

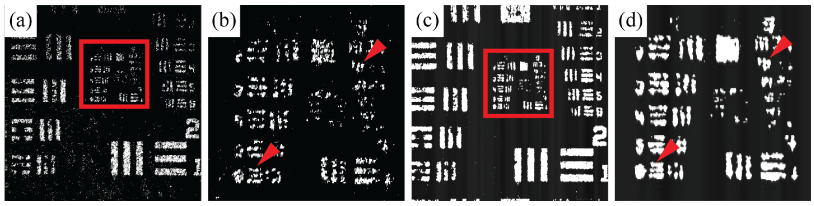

Fig. 4. Comparison of SECSLO and SESLO imaging performance. Images of USAF 1951 test chart through a uniformly scattering layer acquired using (a), (b) a single-mode optical circulator and (c), (d) a DCFC show identical smallest resolvable elements (horizontal: Group 5 Element 6, 8.77 µm; vertical: Group 6 Element 2, 6.96 µm). Images were acquired at the focal plane of the final scan lens (f_s in Fig. 1(b) and 2). Anisotropic lateral resolution is a result of dominant chromatic aberration in the vertical (spectrally encoded) dimension.

3.2 Speckle contrast reduction

Using the SECSLO and SESLO setup from *Section 3.1*, we imaged a uniformly scattering layer to quantify speckle contrast reduction when using multimode collection. In addition to the single-mode circulator and DCF configurations, we also inserted a 250 m MMF patch cord between the DCFC MMF output and SESLO detection photodiode to increase modal dispersion for additional speckle contrast reduction (Fig. 5). Speckle contrast was calculated as the ratio of the standard deviation of the intensity to the mean. Any contribution from additional noise sources (electronic, detector, RIN, etc.) was removed by calculating speckle contrast on 30-frame averaged scattering data. We do not expect any significant reduction in speckle contrast as a result of frame averaging because the solid scattering phantom imaged produced static speckle patterns. Multimode collection (DCFC) reduced speckle contrast by 3.68x as compared to single-mode (SMF). By increasing the number of propagating modes and modal dispersion using a MMF patch cord, speckle reduction was increased to 5.37x.

Biomedical Optics EXPRESS

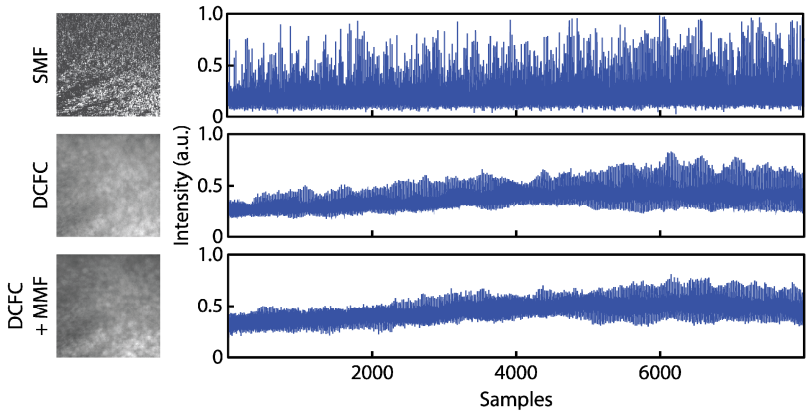

Fig. 5. SESLO speckle reduction using multimode collection. *En face* image and corresponding intensity profiles of a uniformly scattering phantom imaged using single-mode illumination and collection through an optical circulator (SMF), single-mode illumination and multimode collection through a DCFC, and single-mode illumination and multimode collection through a double-clad fiber coupler and a 250 m multimode patch cord (DCFC + MMF).

3.3 In vivo retinal imaging

In vivo human retinal imaging was performed in a 26-year-old volunteer with no known retinal abnormalities under an IRB-approved protocol. SS-SESLO-OCT images were acquired over a 10° FOV centered at the optic nerve (Fig. 6). Raw SESLO frames (Fig. 6(a)) and OCT fast-axis cross-sections (Fig. 6(d)) were acquired at 200 fps. SESLO images were intensity normalized and bandpass filtered to remove residual laser sweep modulation and detector noise. SESLO frames with retina outside the FOV were also acquired and subtracted from all retinal images to remove background from out-of-focus scatterers and specular reflection (Fig. 6(a), 6(b), arrow). Two-dimensional rigid body registration was performed (DFT registration) [53] prior to averaging (Fig. 6(b)). *En face* SESLO and OCT volume projection (Fig. 6(b), 6(c)) show co-registered FOVs.

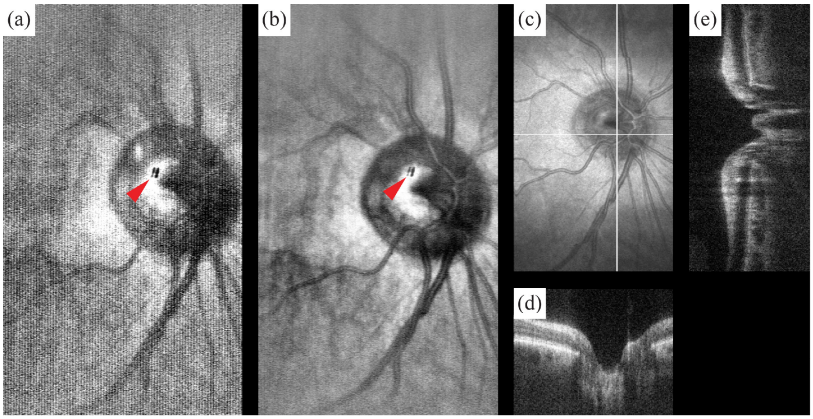

Fig. 6. *In vivo* SS-SESLO-OCT human retinal imaging. (a) Raw SESLO sampled with 1376 (spectral) x 500 pix. acquired at 200 fps and (b) 5-frame average (see Visualization 1). (c) Inherently co-registered volumetric OCT data set with representative (d) fast and (e) slow axis cross-sectional images. (d) B-scans were acquired simultaneously with each SESLO frame. OCT volume was sampled with 1376 x 500 x 500 pix. (spectral x A-scan x B-scan) with a total acquisition time of 2.5 s. Arrow, specular reflection artifact.

Biomedical Optics EXPRESS

3.4 Multi-volumetric averaging

Three volumetric data sets of *in vivo* human retina were acquired with the subject moving freely and re-fixating between each acquisition. All SESLO frames were registered to the first frame of the first volumetric data set using methods described in *Section 2.4* (Fig. 7). Rotational and translational motions (Fig. 7(b)) calculated from raw SESLO frames (Fig. 7(a)) showed features corresponding to saccades, ocular drifts, and a period of missing information during a blink (Fig. 7(b), red bar). Bulk motion compensation accuracy was qualitatively verified by averaging all 1500 registered raw SESLO frames from the three SS-SESLO-OCT volumes. No image blurring or loss of features was observed (Fig. 7(c)).

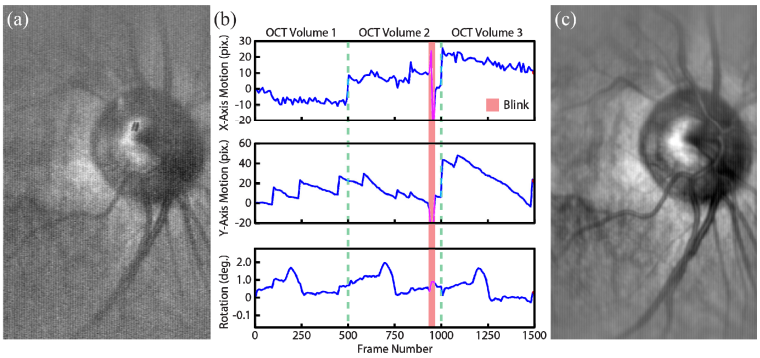

Fig. 7. Multi-volumetric SESLO registration. Three SS-SESLO-OCT volumes were acquired with the subject moving freely and re-fixating between each data set. All SESLO images were registered to (a) the first frame of volume 1 to calculate (b) translational (top and middle) and rotational (bottom) bulk motions (see Visualization 2). (c) Bulk motion compensation and averaging of all 1500 SESLO frames results in significant SNR improvement with no loss of features. Raw SESLO frames were acquired at 200 fps. Each volumetric data set is delineated by dotted lines and a period of missing data during a blink is labeled by the red bar.

All three serially acquired multimodal SS-SESLO-OCT data sets were volumetrically co-registered and combined using mutual information from corresponding *en face* SESLO and cross-section OCT frames. First, fast- and slow-axis scaling factors between SESLO and OCT data were calculated so registration parameters could be directly applied between corresponding frames of each modality. As expected, fast-axis translation and *en face* rotation had unity scaling factors because SESLO and OCT shared a fast-axis scanner and had overlapping and aligned FOVs. A slow-axis translation scaling factor of 2.094 was calculated empirically using features points, including a vessel branch and the optic disc. Fast-axis translations were median filtered to remove noise and applied along with scaled slow-axis translation and rotation offsets to a pixel index grid corresponding to ideal bulk motion free sampling positions. *En face* OCT volume projections using bulk motion compensated sampling indices calculated from SESLO registration parameters clearly shows regions of missing information (Fig. 8(a)-8(c), arrows and asterisk). Each voxel in the OCT data sets was then interpolated to generate one bulk motion compensated multi-volumetric average.

4. Discussion

Our SESLO design theoretically achieves 1616 spectrally resolvable spots. In this study, both SESLO and OCT spectra are sampled using 1376 points as a result of data throughput and digitizer trigger limitations. No loss of SESLO lateral resolution as a result of spectral undersampling was expected or observed (Fig. 4). Ray trace simulations predicted an Airy radius of 7.56 µm and only diffraction-limited performance at the center of the FOV (Fig. 3). Sampling the spectrally encoded dimension using 1376 points would enable Nyquist sampling of twice our maximum FOV with diffraction-limited resolution. Our SESLO resolution is currently limited by wavefront aberrations, which will need to be optimized in future designs.

Biomedical Optics EXPRESS

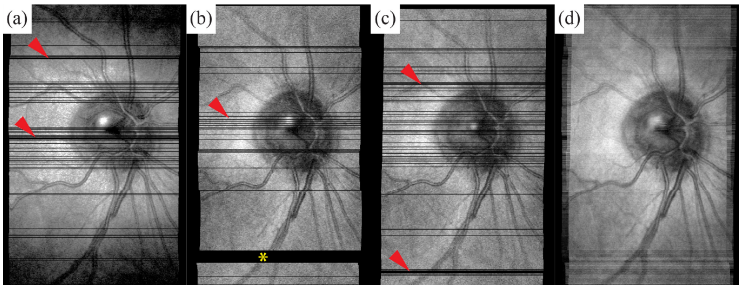

Fig. 8. Multi-volumetric SS-SESLO-OCT registration and mosaicking. (a)-(c) En face projections of volumetric OCT data sets with each B-scan bulk motion corrected using registration parameters calculated from corresponding SESLO frames (Fig. 7). Black lines, missing data; red arrows, saccades and fixation drifts; asterisk, blink. (d) OCT mosaic showing recovery of missing data using mutual information from all three motion-corrected volumes.

4.1 Comparison of SESLO and existing SLO technologies

As described in the Introduction, the SESLO system described in this work is closely related to our previously described SECSLO [49, 50] in design and function. Both SECSLO and SESLO test chart images showed anisotropic lateral resolution as a result of chromatic aberration (Fig. 4). This was also predicted by our optical simulations, which showed spot sizes degrading from diffraction-limited performance at the center of the FOV quicker along the vertical spectrally encoded dimension as compared the horizontal scan axis (Fig. 3). Despite anisotropic lateral resolution, these experiments showed no significant difference in lateral resolution between SECSLO and SESLO, even in the presence of scattering. However, loss of confocality in SESLO may lead to loss of resolution in samples with more complex axial scattering profiles as scatterers from multiple depths within the confocal-gate of the DCF inner cladding are summed axially.

SESLO has several key advantages and disadvantages as compared to CSLO [46–48] and line scanning ophthalmoscope (LSO) [65, 66] technologies. As described in the Introduction, spectral encoding reduces the required scanning axes to one and enables high-speed *en face* imaging without the need for resonant scanners, which are inherently difficult to synchronize and have nonlinear scan trajectories. These advantages come at the expense of confocality and, thus, CSLO has depth-selectivity and better lateral resolution. The lateral motion tracking and registration performance of SESLO described in his manuscript are not affected by lack of axial sectioning as a result of loss of confocality in our detection scheme.

Similar to SESLO, LSO provides high-speed *en face* imaging by using only a single-axis scanning mirror and illuminates the retina through a cylindrical lens to create an extended line-source. In LSO, the scattered light is imaged onto the face of a linear detector array, which acts as a quasi-confocal detector. Axial sectioning and lateral resolution performance in LSO is better than SESLO but worse than that of CSLO. Research and commercial LSO systems have been integrated with OCT for retinal tracking and registration [32, 35, 67] with *en face* frame-rates ranging from 15 to 100 fps as compared to our 200 fps SESLO. Although single-frame LSO image quality is superior to single-frame SESLO, our registration data (Fig. 7) shows single-frame SESLO images have sufficient contrast and features for retinal tracking and registration at 200 fps. The main drawback of LSO, however, is its frame-rate is determined by the number of pixels read out on the linear detector, which results in an inherent trade-off between imaging speed and sampling density. Additionally, LSO uses a free space bulk optics relay between the source, sample, and detector, which necessitates a change in detection optics to adjust image sampling density.

4.2 Speckle contrast reduction

Theoretical calculations of the number of modes and modal dispersion based on inner cladding specifications of the DCF predicted a 1.9x reduction in speckle contrast as compared

Biomedical Optics EXPRESS

to single-mode collection. However, our measurements showed a contrast reduction of 3.68x (Fig. 5). This disparity may be attributed to a combination of factors. First, the DCFC consists of DCF fused to MMF [51], which is coupled directly to the SESLO photodiode in our system (Fig. 1(a)). The MMF has both a larger NA (0.26) and core diameter (200 μm), which supports more spatial modes as compared to the DCF inner cladding and, thus, may provide additional speckle contrast reduction. Second, our calculations only considered incoherent averaging of spatial modes collected from a point source, which is an incomplete approximation when considering focused spot point-spread-functions and multiple scattering. Similarly, additional illumination modes will also affect scattered light collection and, therefore, speckle contrast. In our design, a single-mode light source is coupled to the single-mode core of the DCFC. Initially, both SMF and DCF ends were connectorized and coupled mechanically using index-match gel. However, we observed significant light coupling into the inner cladding of the DCF at the image plane. Most recently, we fusion spliced a length of SMF to the DCF core, which significantly reduced light coupling to the DCF inner cladding, but SESLO illumination is not completely single-mode.

When adding an additional 250 m of MMF to our SESLO collection arm, theory predicted 21x speckle contrast reduction as compared to single-mode SECSLO imaging. Our measurements only showed a 5.37x reduction when imaging a uniformly scattering phantom. This was likely because the scattered light was not evenly distributed between all spatial modes supported by the DCF and MMF. Intermediate apertures along our SESLO optical path would spatially filter the scattered light, thus, limiting both the number of modes collected and collection efficiency of the DCF. Both of these limitations may be addressed by redesigning the optical relay to accommodate the entire NA and core diameter of the DCF inner cladding.

4.3 In vivo retinal imaging

In vivo multimodal SS-SESLO-OCT imaging has a FOV that is limited to ~10° at the retina (Fig. 6). This is approximately half of the full-field predicted by our optical design (Fig. 3) and is predominately constrained by clipping at the shared scan lens (f_s in Fig. 1(b) and 2). While significantly smaller than that of conventional SLOs, SS-SESLO-OCT FOV may be scaled arbitrarily by adjusting the magnification of the imaging relay and is only limited by practical system size considerations. Additionally, SESLO SNR falls-off quickly outside of the central 10° because of a combination of off-axis aberrations and spectral shape of swept-laser. Raw SESLO image SNR is also limited by strong specular reflections from lens and fiber faces. Without confocal or coherent gating and with increased optical throughput with multimode collection, air-to-glass interface reflections dominated the dynamic range of our amplifiers and digitizers. Lens face reflections were partially mitigated by redesigning the imaging relay to minimize the number of surfaces at intermediate SESLO image planes. Additionally, several SESLO images were acquired with the retina out of the FOV and subtracted from all raw SESLO frames in post-processing (Fig. 6). Here, residual background subtraction artifacts are present (Fig. 6(a), 6(b), red arrows) at locations where the lens face reflection saturated the digitizer.

En face retinal SESLO images showed increased SNR and reduced noise but significantly higher background noise as compared to SECSLO. Corresponding OCT volume projections (Fig. 6(e)) showed higher contrast and resolution as a result of confocal and coherent gating. Certain structural features, such as the surface of the retina, are also better depth-resolved on OCT. However, because each SESLO *en face* frame was acquired 500x faster than each *en face* OCT volume projection, SESLO images were free of the motion artifacts and regions of missing data (Fig. 8(f), arrows and asterisk) observed on OCT. Similarly, lack of depth-resolved imaging also benefits visualization of deep retinal features using SESLO, such as the choroidal vasculature that is readily visible on both the raw and averaged frames (Fig. 7).

Biomedical Optics EXPRESS

4.4 Multi-volumetric averaging

The signifance of concurrent multimodality imaging of overlapping FOVs in the eye is to benefit real-time image aiming and to provide complementary bulk motion information for volumetric registration and averaging in post-processing. Average of all three motion-corrected OCT volumes (Fig. 8(d)) shows recovery of these regions using mutual information from serially acquired volumes and reduced noise as a result of averaging during interpolation. Here, the empirically calculated scaling parameters between SESLO and OCT FOVs compensated for the difference in sampling density along the SESLO spectrally encoded dimension (1376 minus vignetted regions at the top and bottom of the FOV) and OCT fast-axis (500 pix.). We believe our method for applying established computationally efficient DFT and APT image registration methods on *en face* SESLO images, which are acquired hundreds of times per OCT volume and contain more than a thousand times less information, may significantly reduce the computational complexity or enable real-time volumetric registration of corresponding OCT volumes. The registration and averaging algorithms described here may also be applied for mosaicking of multiple overlapping fields for extended FOV imaging.

This technology has direct clinical implications in many ocular pathologies. Visualization and analysis of widefield pathology including the presence of vascular malformations, neovascularization and capillary non-perfusion has changed our current grading of diabetic retinopathy. Up to 20% of eyes have a higher level of retinopathy when evaluating ultra-widefield retinal images when compared to standard ETDRS 7-field photos [68]. Eyes with predominantly peripheral lesions have a 4.7-fold increased risk of progression to proliferative diabetic retinopathy [69], which motivates the clinical need for accurate widefield mosaicking methods especially when combined with OCT-A. In addition, widefield mosaics will permit more thorough peripheral retinal diagnostic evaluations for genetic diseases [70]. Finally, a robust multimodal SS-SESLO-OCT system will enhance current intraoperative OCT capabilities by permitting real-time surgical feedback and instrument tracking.

5. Conclusions

SS-SESLO-OCT is a novel simultaneous multimodal ophthalmic imaging system that enables concurrent acquisition of SESLO and OCT data with inherently co-registered FOVs. We took advantage of the complementary information from *en face* SESLO and cross-sectional OCT frames to perform volumetric registration and motion compensation using computationally efficient APT and DFT cross-correlation. We demonstrated our registration and averaging method on three in vivo human retinal SS-SESLO-OCT data sets and showed recovery of missing data using mutual information from serially acquired volumes. Using complementary information from SESLO and OCT, we demonstrated multi-volumetric registration and averaging to recover regions of missing data resulting from blinks, saccades, and ocular drifts using mutual information from serially acquired volumes. This preliminary study shows the utility our registration method for multi-volumetric motion compensation and averaging, which may be directly applied for widefield mosaicking and vascular mapping with potential applications in ophthalmic clinical diagnostics, handheld imaging, and intraoperative guidance.

Funding

This research was supported by Vanderbilt University start-up funds, Ohio Department of Development grant TECH-13-059, and US National Institutes of Health National Eye Institute grant R01EY023039. The content is solely the responsibility of the authors and does not necessarily represent the official views of the National Institutes of Health.

Acknowledgments

We thank Castor Optics for providing a prototype 1060 nm double-clad fiber coupler. The majority of the work described in this manuscript was performed at Cleveland Clinic.